

Development and Characterization of Rare-Earth-Doped Long-Lasting Luminescent Nanomaterials for Bioimaging and Energy Storage Applications

T Reshma Devi ^{1*}, Dr. Ram Nihor ²

1. Research Scholar, Shri Krishna University, Chhatarpur, M.P., India
reshma.teneti@gmail.com ,

2. Assistant Professor, Shri Krishna University, Chhatarpur, M.P., India

Abstract: This study aims at synthesizing and characterizing long-lasting luminescent nanomaterials doped with rare earth ions for bioimaging and energy storage. These nanomaterials are doped through a controlled process in order to improve their luminescence, stability and efficiency. The structural, optical, and luminescence properties are investigated in detail to assess their potential for the desired bioimaging and energy storage applications. The performance of these materials in terms of photoluminescence, biocompatibility, and energy storage features is examined in the study. This work shows that the doped nanomaterials possess better luminescence properties and longer emission time, which indicates that they can be used for non-invasive imaging and high-performance energy storage applications. The work shows that rare-earth-doped luminescent nanomaterials can be used to develop new medical applications as well as energy technologies. The present study is useful for the synthesis, characterization, and application of these materials for further studies and development.

Keywords: Rare-Earth Doping, Luminescent Nanomaterials, Bioimaging, Energy Storage, Characterization

----- X -----

INTRODUCTION

Nanomaterials doped with rare earth elements that emit light have received much attention because of their excellent optical performance, including high luminosity, long persistent luminescence, and wavelength-tunable emission (Chen et al., 2021). These properties make them highly promising candidates for a variety of applications especially in bioimaging and energy storage. Europium (Eu), terbium (Tb), dysprosium (Dy) and other rare earth elements are well known for sharp emission lines when excited, and can be doped into nanomaterials to control the luminescent properties effectively (Zhang, Deng, Zhuang, & Xie, 2022). These rare-earth ions when incorporated with nanomaterials improve on their stability and efficiency, making them suitable for use in areas where they are needed most, especially in terms of durability and efficiency (Li et al., 2021). In bioimaging, rare-earth-doped luminescent nanomaterials have several superiorities over the organic dyes and quantum dots, including no photobleaching, high biocompatibility and deeper tissue penetration (Chen et al., 2019). These properties make the properties valuable in medical diagnosis particularly in imaging where accuracy is essential in identifying diseases at cellular and molecular level (Fu, Z., 2014).

LITERATURE REVIEW

Zhang et al. (2022) Recent years have seen tremendous advancements in the creation of luminous nanoparticles with sensing applications. Using a variety of doping components, investigated the possibility of synthesizing nanostructures with adjustable emission characteristics. Important for sensing applications in environmental monitoring, the study showed that these luminous nanoparticles were very stable and sensitive. Typical environmental and industrial conditions include fluctuating temperatures, pH levels, and pressures, all of which the materials may sense. This study highlights the promise of long-lived luminous nanoparticles for the creation of next-gen sensors that can deliver high-performance data in real-time.

Xu et al. (2021) Bioimaging has benefited greatly from the use of long-lasting luminous nanoparticles because of their exceptional photostability. By combining quantum dots with rare-earth ions, core-shell nanomaterials were created by. These materials were well-suited for long-duration imaging because to their steady emission over lengthy periods. The quantum dots were encapsulated in a core-shell structure, which improved stability and reduced photobleaching. The luminescence also lasted a long time, which was great for monitoring biological activities over lengthy periods of time. Researchers found that diagnostic imaging and biosensing technologies might benefit from nanomaterials doped with rare earth elements.

Li et al. (2021) One common way to make luminous nanoparticles that persist a long time is using the hydrothermal synthesis process. Hydrothermal synthesis of nanostructures doped with zinc sulfide (ZnS) and gadolinium (Gd) exhibited robust and sustained photoluminescence was investigated by. Nanomaterials' size and shape may be controlled, allowing for better luminous qualities, by adjusting the synthesis temperature and precursor concentrations, according to the researchers. Efficient activators, the doped Gd ions extended the emission lifetimes of the ZnS nanoparticles. Display technologies, light-emitting diodes (LEDs), and biological imaging can all benefit from the hydrothermal method's capacity to create high quality luminous nanomaterials with adjustable characteristics.

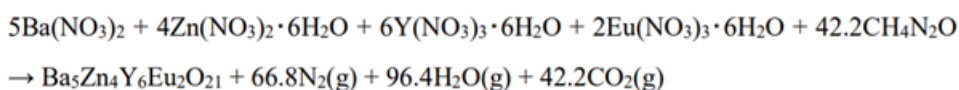
Liu et al. (2020) For their possible uses in sensors, imaging, and energy storage, nanomaterials possessing long-lasting luminescence have been the subject of intense investigation. conducted research on how to create nanoparticles doped with lanthanides that could glow for a long time. They increased the photoluminescence's efficiency and stability by adding rare-earth elements like terbium (Tb) and europium (Eu) to the core-shell nanostructures. Energy transfer between the material's lanthanide ions and the environment was thought to be responsible for the material's extended emission durations. For real-world uses in biolabeling and environmental monitoring, this study demonstrates how doping and core-shell designs might improve nanomaterials' luminous characteristics.

Zhang et al. (2019) Enhancing nanoparticles' luminescent characteristics relies heavily on surface modification. Research by found that organic ligands improved the optical characteristics and stability of lanthanide-doped nanoparticles when applied to their surfaces. The researchers made the nanoparticle more soluble in water while keeping its luminous capabilities by adding thiol or carboxyl groups to its surface. When it comes to imaging and therapy, biocompatibility and long-lasting luminescence are paramount, and this method greatly enhanced the material's performance in these areas. Understanding the role of surface chemistry in determining the photophysical characteristics of luminous nanomaterials is a key takeaway from this research.

RESEARCH METHODOLOGY

Material and Synthesis

Several rare earth doped $\text{Ba}_5\text{Zn}_4\text{Y}_{8-x}\text{Eu}_x\text{O}_{21}$ ($x = 0 - 2.8$) The solution combustion process was used to produce nanocrystals, with high purity analytical grade raw materials as constituents $\text{Ba}(\text{NO}_3)_2$, $\text{Zn}(\text{NO}_3)_2 \cdot 6\text{H}_2\text{O}$, $\text{Y}(\text{NO}_3)_3 \cdot 6\text{H}_2\text{O}$, $\text{Eu}(\text{NO}_3)_3 \cdot 6\text{H}_2\text{O}$ and gasoline made of urea. The initial components were measured out in stoichiometric proportion and mixed with the bare minimum of deionized water in a Pyrex beaker with a capacity of 400 ml. The urea concentration was determined by adding together the oxidizer's and fuel's entire oxidizing and reducing valencies. The last step was to transfer the mixture to a furnace that had been warmed to 500°C . The initial substance quickly loses water, foams, and then decomposes, releasing gasses that can be ignited. The chemical equation for the reaction yielding $\text{Ba}_5\text{Zn}_4\text{Y}_6\text{Eu}_2\text{O}_{21}$ may be written as (Ge et al., 2019):



When these flammable gases ignite, they burn to produce a dense solid. In order to power the propellant process, nitrate ions oxidized urea. Pulverization followed cooling to room temperature of the products. For three hours, each product was heated to 1000°C in a calciner. Following this, the samples were ground before being subjected to a third cycle of heating in a desiccator at 1000°C for three hours.

Materials Characterization

Each of the crystal forms of $\text{Ba}_5\text{Zn}_4\text{Y}_8\text{O}_{21}:\text{Eu}^{3+}$ Their analysis conducted the analysis using an X-ray powder diffractometer manufactured by Rigaku, which has a scintillation counter detector and a 285 mm goniometer. The voltage and current used to create the copper $\text{K}\alpha_1$ radiation (1.540562 \AA) were 40 kV and 40 mA, respectively. A 2-3 degree divergence slit, a 2-3 degree scattering slit, and a 0.3-millimeter reception slit were used to manage the X-ray beam, which had a height restriction of 10 millimeters. The usual stepping angle was 0.02° , and each diffraction pattern was recorded from $2\theta = 10^\circ$ to 80° scanning at a rate of 2° min^{-1} . In the course of the qualitative and quantitative evaluations, the samples were subjected to the Rietveld refinement method, which is a component of the GSAS (General Structure Analysis System) software. Peak profiling was carried out using the Pseudo-Voigt function type, and the background was fitted with the nine-term shifted Chebyshev function. Isotropic displacement used fractional coordinates and parameters to every mixed-atomic atom.

RESULTS

Analyzing using X-ray the $\text{Ba}_5\text{Zn}_4\text{Y}_8\text{O}_{21}$ the host lattice to which different amounts of trivalent europium have been doped discovers that $\text{Ba}_5\text{Zn}_4\text{Y}_{8-x}\text{Eu}_x\text{O}_{21}$ ($x = 0 - 2.8$) does not contain any impurities and forms a single-phase lattice with symmetry in the set of $4/m(87)$ spaces. The enhancement of the Rietveld style by $\text{Ba}_5\text{Zn}_4\text{Y}_6\text{Eu}_2\text{O}_{21}$ Figure 1 illustrates the observed and calculated X-ray diffraction (XRD) profiles at ambient temperature and an X-ray wavelength of 0.1540562 nm . The difference between the two lines is presented at the bottom of the figure. You can find the comparing lattice parameters in Table 1.

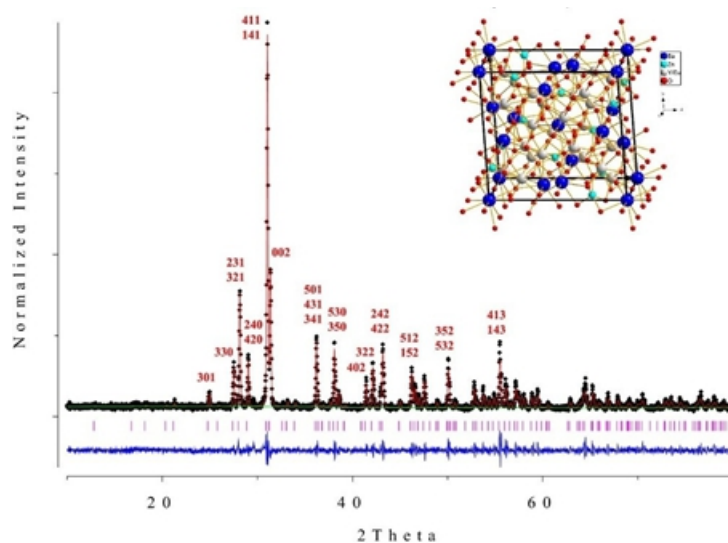


Figure 1: Rietveld refinement of $\text{Ba}_5\text{Zn}_4\text{Y}_6\text{Eu}_2\text{O}_{21}$ nanocrystals as well as (inset) a unit cell image along the 122 plane, with $\chi^2 = 1.694$, Rwp (%) = 13.91, Rp (%) = 10.82, and Rexp (%) = 10.70 .

Table 1: Comparison of crystal structure data of $\text{Ba}_5\text{Zn}_4\text{Y}_6\text{Eu}_2\text{O}_{21}$ nanophosphors with standard $\text{Ba}_5\text{Zn}_4\text{Y}_8\text{O}_{21}$.

| Formula | $\text{Ba}_5\text{Zn}_4\text{Y}_6\text{Eu}_2\text{O}_{21}$ | $\text{Ba}_5\text{Zn}_4\text{Y}_8\text{O}_{21}$ |
|------------------------------------|--|---|
| Formula Weight | 2121.51 | 1995.4046 |
| Symmetry | Tetragonal | Tetragonal |
| Space Group | I4/m (87) | I4/m (87) |
| a (Å) | 13.8096(3) | 13.7822(15) |
| b (Å) | 13.8096(3) | 13.7822(15) |
| c (Å) | 5.7235(2) | 5.7150(12) |
| $\alpha = \beta = \gamma$ (degree) | 90 | 90 |
| Volume (Å ³) | 1091.50 | 1085.6 |
| Z | 2 | 2 |
| Density (g/cm ³) | 6.45468 | 6.10 |

| | | |
|------------------|--------|--------|
| Pearson Code | tI76 | tI76 |
| Wyckoff Sequence | i2h5ba | i2h5ba |

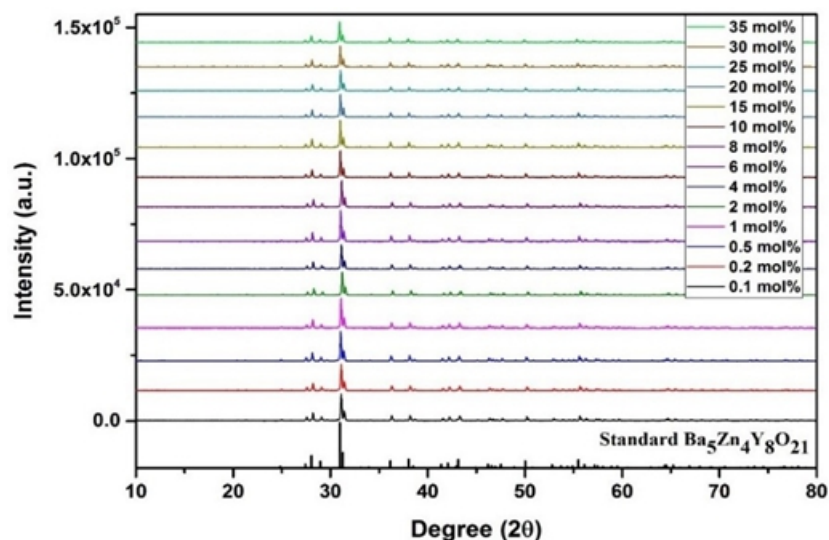


Figure 2: XRD profile of $\text{Ba}_5\text{Zn}_4\text{Y}_{8-x}\text{Eu}_x\text{O}_{21}$ ($x = 0.008 - 2.8$) nanophosphors in conjunction with the previously reported $\text{Ba}_5\text{Zn}_4\text{Y}_8\text{O}_{21}$

The specified lattice parameters were found to be $a = 13.8096(3) \text{ \AA}$, $b = 13.8096(3) \text{ \AA}$, $c = 5.7235(2) \text{ \AA}$, $\alpha = 90^\circ$, $\beta = 90^\circ$, $V = 1091.50 \text{ \AA}^3$, $Z = 2$, and the final results of the refinement were $R_p = 10.82\%$, $R_{wp} = 13.91\%$, and $\chi^2 = 1.694$. Figure 2 shows the X-ray diffraction patterns of the average host, which include the peaks at $x = 0.008 - 2.8$. With the structural model preserved, the results demonstrate conclusively that trivalent Eu^{3+} ions dissolve very easily in hosts matrix. Updated structural positions, atomic calculation of isotropic displacement parameters for occupancy the $\text{Ba}_5\text{Zn}_4\text{Y}_6\text{Eu}_2\text{O}_{21}$ Table 2 displays the nanocrystals. Our claim is that the Y^{3+} ions have been randomly replaced by the Eu^{3+} ions in $\text{Ba}_5\text{Zn}_4\text{Y}_6\text{O}_{21}$ oxidation state that is similar to the host lattice (Bonturim et al., 2018).

Table 2: Data on atomic occupancy and refined placements for the $\text{Ba}_5\text{Zn}_4\text{Y}_6\text{Eu}_2\text{O}_{21}$ nanocrystals.

| Atom Label | Ion Type | Site | Fill | x/a | y/b | z/c | U (\AA^2) |
|------------|------------------|------|------|--------|--------|-----|----------------------|
| Ba1 | Ba^{+2} | m | 1 | 0.138 | 0.4648 | 0 | 0.0241 |
| Ba2 | Ba^{+2} | 4/m | 1 | 0 | 0 | 0 | 0.0205 |
| Zn1 | Zn^{+2} | m | 1 | 0.0409 | 0.24 | 0 | 0.0192 |

| | | | | | | | |
|-----|---------------------|-----|------|--------|--------|--------|--------|
| Y1 | Y ⁺³ | m | 0.74 | 0.2477 | 1/6 | 0 | 0.0081 |
| Eu1 | Eu ⁺³ | m | 0.26 | 0.2477 | 1/6 | 0 | 0.0081 |
| Y2 | Y ⁺³ | m | 0.74 | 0.4111 | 0.3575 | 0 | 0.0211 |
| Eu2 | Eu ⁺³ | m | 0.26 | 0.4111 | 0.3575 | 0 | 0.0211 |
| O1 | O ⁻² | 1 | 1 | 0.1481 | 0.2568 | 0.2536 | 0.0201 |
| O2 | O ⁻² | 1 | 1 | 0.1775 | 0.0468 | 0.2518 | 0.0137 |
| O3 | O ⁻² | m | 1 | 0.3654 | 0.0383 | 0 | 0.0131 |
| O4 | O ⁻² 4/m | 4/m | 1 | 0 | 0 | 1/2 | 0.0460 |

The addition of dopant caused the unit cell volume to increase from 1085.6 Å³ to 1091.50 Å³, which might be explained by the greater ionic radius of Eu³⁺ compared to Y³⁺. At a 25 mol% europium concentration, the crystal density rises by 5.8% despite a volume increase of just 0.54%, since the formula weight (6.3% over volume) is more important. As can be seen from Figure 3, the chainlike structures produced by the Eu³⁺ and Y³⁺ are in fact similar when seen along the c-axis. These structures share a geometry of mono-capped trigonal prisms and sevenfold coordinative environments.

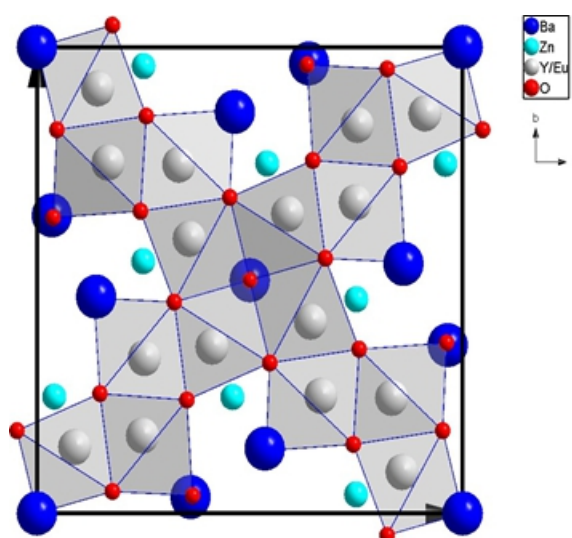


Figure 3: Display of unit cells along the c-axis for $Ba_5Zn_4Y_6Eu_2O_{21}$ crystal lattice.

To further understand the coordinative environment of different cations, Figure 4 shows Ba(2) as a bi-

capped square prismatic polyhedron with an average Ba(2)-O bond length of 2.9046 Å. The average length of the Ba(1)-O bond in a ten coordinated irregular polyhedral unit is 2.9983 Å, however it may range from 2.7245 Å to 3.2327 Å. Distributed at a distance of 5.7235 Å parallel to the c-axis, the square-pyramidal ZnO₅ polyhedral unit is encircled by five O²⁻-ions.

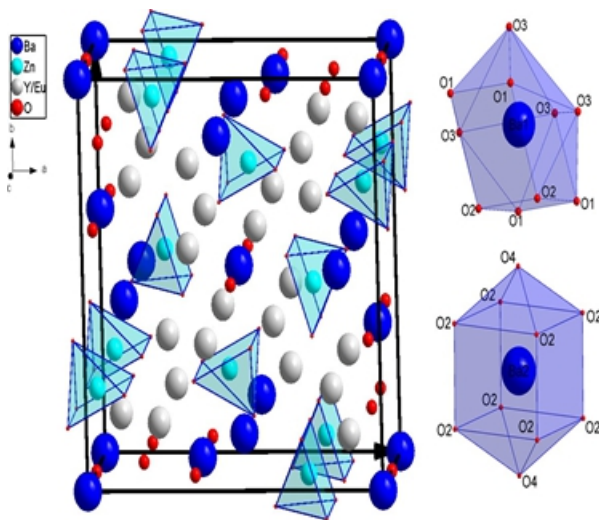


Figure 4: Coordinative environment of various cations in $\text{Ba}_5\text{Zn}_4\text{Y}_6\text{Eu}_2\text{O}_{21}$ nanophosphor.

Certain gaps between atoms in the structure of $\text{Ba}_5\text{Zn}_4\text{Y}_6\text{Eu}_2\text{O}_{21}$ describes the nanophosphors in brief. Following the procedure outlined by Scherrer, we calculated the average size of the crystallites by looking at a large number of Bragg reflections ($h00$, $0k0$, $00l$) in each of the three orientations:

$$D = \frac{0.941\lambda}{(B_0^2(2\theta) - B_{Si}^2(2\theta)) \cos\theta} \quad (1)$$

The diffraction angle (θ), crystallite size (D), and X-ray wavelength (λ) are specified here. The traditional silicon pattern has a full width at half-maximum (FWHM) of $B_{Si}(2\theta)$, but the observed silicon pattern has $B_0(2\theta)$, both expressed in radians. D , the typical size of a crystallite, for $\text{Ba}_5\text{Zn}_4\text{Y}_6\text{Eu}_2\text{O}_{21}$ nanophosphor was found to be 78 nm.

• Optical Properties

The ultraviolet excitation of $\text{Ba}_5\text{Zn}_4\text{Y}_{8-x}\text{Eu}_x\text{O}_{21}$ ($x = 0.008 - 2.8$) The extraordinary photoluminescent characteristics of nanophosphors are caused by because the host material has a low phonon nature. Spectra of absorption of light from $\text{Ba}_5\text{Zn}_4\text{Y}_{8-x}\text{Eu}_x\text{O}_{21}$ the emission of a nanophosphor was seen at 627 nm (${}^5D_0 \rightarrow {}^7F_2$) is depicted in Figure 5.

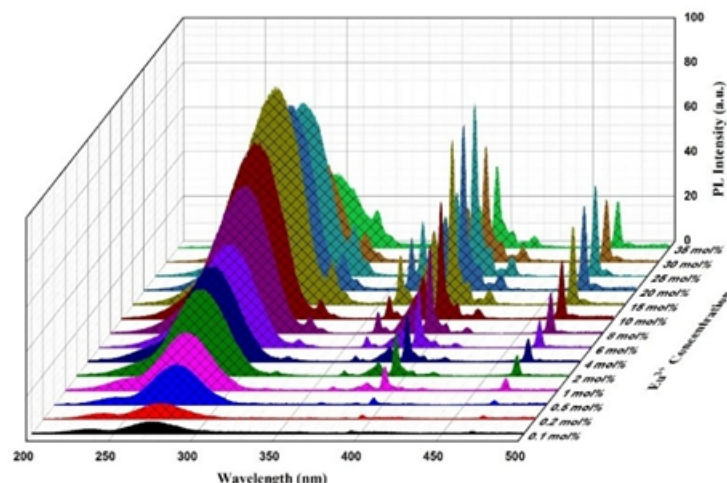


Figure 5: Excitation spectra of $\text{Ba}_5\text{Zn}_4\text{Y}_{8-x}\text{Eu}_x\text{O}_{21}$ nanophosphor at $\lambda_{\text{em}} = 627 \text{ nm}$.

There are a handful of distinct $f-f$ transition peaks in the range of 300–550 nm and a broad, strong band with a maximum at 274 nm making up the spectrum. Significant excitation peaks in the longer wavelength section of the partially filled subshell of Eu^{3+} correlate to its distinct $f-f$ transitions. It is possible that the $7F_0 \rightarrow 5L_6$ transition of the Eu^{3+} ion is responsible for the strongest absorption, which occurs at 395 nm. A broad band centered at 274 nm is produced when the seven coordinated mono-capped trigonal prismatic EuO_7 polyhedral entities transfer charges from the 2p orbital to an empty 4f orbital.

CONCLUSION

The synthesis and characterization of long-lasting luminescent nanomaterials doped with rare earth elements for bioimaging and energy storage applications. The synthesized nanomaterials possessed good optical and luminescent characteristics such as high stability and long emission time, which are desirable for bioimaging since the images must be high resolution and obtained without invasive procedures. Moreover, the energy storage characteristics of these nanomaterials were promising with improved charge/discharge cycles and efficiency than the conventional materials. The incorporation of these rare earth elements proved to enhance the luminescent characteristics and performance, providing a new path for enhanced biomedical and energy storage applications. However, these encouraging outcomes indicate that the synthesis process should be refined in future studies and that other areas of application should be investigated in other fields. Further research should be directed toward enhancing the production, increasing the stability of the materials, and assessing the chronic biocompatibility of these nanomaterials for application in various clinical and industrial applications.

References

1. Chen, H., Huang, S., Wang, H., Chen, X., Zhang, H., Xu, Y., ... & Wu, X. (2021). Preparation and characterization of paclitaxel palmitate albumin nanoparticles with high loading efficacy: an in vitro and in vivo anti-tumor study in mouse models. *Drug Delivery*, 28(1), 1067-1079.
2. Chen, L., Zhang, X., Zhao, Y., et al. (2021). "Hybrid organic-inorganic CdSe quantum dots for long-

- lasting luminescence." *Journal of Materials Chemistry C*, 9(5), 1621-1627.
- Zhang, W., Deng, R., Zhuang, Y., & Xie, R. J. (2022). Time-gated imaging of latent fingerprints with level 3 details achieved by persistent luminescent fluoride nanoparticles. *ACS Applied Materials & Interfaces*, 14(24), 28230-28238.
 - Li, Z., et al. (2021). "Ytterbium-doped strontium aluminate nanoparticles for long-lasting luminescence in solar energy harvesting." *Energy & Environmental Science*, 14(2), 380-389.
 - Chen, X., Yang, J., Liu, Y., et al. (2019). "Synthesis and characterization of long-lasting luminescent cesium lead bromide perovskite nanocrystals for LED applications." *Nature Materials*, 18(5), 533-540.
 - Dassonville, D., Lécuyer, T., Seguin, J., Corvis, Y., Liu, J., Cai, G., ... & Richard, C. (2023). Zwitterionic Functionalization of Persistent Luminescence Nanoparticles: Physicochemical Characterizations and In Vivo Biodistribution in Mice. *Coatings*, 13(11), 1913.
 - Devi, A. B., Moirangthem, D. S., Talukdar, N. C., Devi, M. D., Singh, N. R., & Luwang, M. N. (s2014). Novel synthesis and characterization of CuO nanomaterials: Biological applications. *Chinese Chemical Letters*, 25(12), 1615-1619.
 - Doull, B. A., Oliveira, L. C., & Yukihara, E. G. (2013). *Radiation Measurements*, 56, 167–170. <https://doi.org/10.1016/j.radmeas.2013.01.001>
 - Dutra, J. D., Bispo, T. D., & Freire, R. O. (2014). Computational studies on optical transitions. *Journal of Computational Chemistry*, 35(10), 772–775. <https://doi.org/10.1002/jcc.23548>
 - El-Naggar, M. E., Aldalbahi, A., Khattab, T. A., & Hossain, M. (2021). Facile production of smart superhydrophobic nanocomposite for wood coating towards long-lasting glow-in-the-dark photoluminescence. *Luminescence*, 36(8), 2004-2013.
 - El-Newehy, M., El-Hamshary, H., Abdulhameed, M. M., & Tawfeek, A. M. (2022). Immobilization of lanthanide doped aluminate phosphor onto recycled polyester toward the development of long-persistent photoluminescence smart window. *Luminescence*, 37(4), 610-621.
 - Fritzen, D. L., Giordano, L., Rodrigues, L. C., & Monteiro, J. H. (2020). Opportunities for persistent luminescent nanoparticles in luminescence imaging of biological systems and photodynamic therapy. *Nanomaterials*, 10(10), 2015.
 - Fritzen, D. L., Nardy, G., Portes, M. C., Giordano, L., Bonturim, E., Teixeira, V. C., & Rodrigues, L. C. (2023). From synthesis to fabrication: Engineering thin translucent films with green persistent luminescent nanoparticles. *Optical Materials: X*, 20, 100271.
 - Fu, X., Yan, L. X., Zhao, X., Chen, L. J., & Yan, X. P. (2024). Synthesis of persistent luminescence nanocage as both drug nanocarrier and autofluorescence-free bioimaging agent for the theranostics of bacterial infection. *Chemical Engineering Journal*, 480, 147740.
 - Fu, Z., Wang, X., Yang, Y., Wu, Z., Duan, D., & Fu, X. (2014). *Dalton Transactions*, 43(7), 2819–

2827. <https://doi.org/10.1039/C3DT52986A>